HHS Public Access

Author manuscript

Structure. Author manuscript; available in PMC 2018 February 07.

Published in final edited form as:

Structure. 2017 February 07; 25(2): 317–328. doi:10.1016/j.str.2016.12.006.

Co-folding of a FliF-FliG split domain forms the basis of the MS:C ring interface within the bacterial flagellar motor

Michael J. Lynch[1], **Robert Levenson**[2], **Eun A Kim**[3], **Ria Sircar**[1], **David F. Blair**[3], **Frederick W. Dahlquist**[2], and **Brian R. Crane**[1,4,*]

[1]Department of Chemistry and Chemical Biology, Cornell University, Ithaca, New York, 14853, USA

[2]Department of Chemistry and Biochemistry, University of California Santa Barbara, Santa Barbara, California 93106-9510, USA

[3]Department of Biology, University of Utah, Salt Lake City, Utah 84112, USA

Summary

The interface between the membrane (MS) and cytoplasmic (C) rings of the bacterial flagellar motor couples torque generation to rotation within the membrane. The structure of the C-terminal helices of the integral membrane protein FliF ($FliF_C$) bound to the N-terminus of the switch complex protein FliG ($FliG_N$) reveals that $FliG_N$ folds around $FliF_C$ to produce a topology that closely resembles both the middle and C-terminal domains of FliG. The interface is consistent with solution-state NMR, SAXS, *in vivo* interaction studies and cellular motility assays. Co-folding with $FliF_C$ induces substantial conformational changes in $FliG_N$, and suggests that FliF and FliG have the same stoichiometry within the rotor. Modeling the $FliF_C$:$FliG_N$ complex into cryoEM rotor density updates the architecture of the middle and upper switch complex and shows how domain shuffling of a conserved interaction module anchors the cytoplasmic rotor to the membrane.

eTOC Blurb

FliF and FliG comprise the MS-ring and upper C-ring of the bacterial flagellar motor. Lynch et al. use X-ray crystallography, SAXS, NMR, and *in vivo* studies to reveal how FliF:FliG fold into a

*Correspondence: bc69@cornell.edu (B.R.C.).
[4]Lead Contact

Conflict of Interest
The authors declare no conflict of interest.

Accession Numbers
$FliF_C$:$FliG_N$ complex PDB ID: 5TDY
$FliF_C$:$FliG_N$ NMR assignments BMRB ID: 26908

Author Contributions
Conceptualization: B.R.C., F.W.D. D.F.B.; Methodology, R.L., M.J.L.; Investigation: M.J.L., R.L., E.K., and R.S.; Writing – Original Draft: M.J.L. and B.R.C. (*In vivo* data/discussion – E.K. and D.F.B., NMR data/discussion – R.L. and F.W.D.); Writing – Review & Editing: M.J.L., R.L., B.R.C., F.W.D., D.F.B., and R.S.; Funding Acquisition, Resources, and Supervision: B.R.C., F.W.D., and D.F.B.

single domain, whose toplogy is found elsewhere in FliG, and generate an updated model of the upper flagellar rotor.

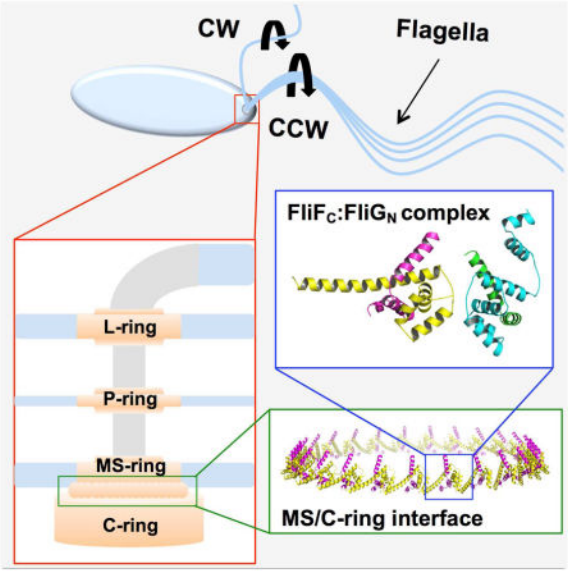

Keywords

switch complex; flagellar motor; domain shuffling

Introduction

The bacterial flagellar motor is the principle organelle that enables motile bacteria to move within their environment. The motor can be divided into three major components: (1) the filament, which serves as the propeller of the motor, (2) the hook, a flexible adaptor between the filament and cell body, and (3) the basal body, which generates torque and induces flagellar rotation switching. The basal body (Figure 1) is comprised of a series of transmembrane rings that enclose a central rod. Powered by the proton or sodium gradient that spans the inner membrane, torque is generated by interactions between the membrane-embedded ion channels and the switch complex located in the cytosolic space (Berg, 2003; Minamino *et al.,* 2008, 2015; Sowa, 2008; Chen *et al.,* 2011) The switch complex forms the C-ring and is composed of the proteins FliG, FliM, and FliN (or FliY) (Figure 1). The switch complex rotates either counterclockwise (CCW) or clockwise (CW) and in doing so dictates whether the cell swims smoothly or tumbles in solution. Interaction of the switch complex with the phosphorylated form of the response regulator CheY causes switching of rotation direction (Berg, 2003; Sowa, 2008).

A prerequisite for motor operation and assembly during the early stages of flagellar biosynthesis is the correct positioning of the switch complex relative to the MS-ring (Macnab, 2003; Grünenfelder *et al.,* 2003; Chevance *et al.,* 2008; Minamino *et al.,* 2008, 2015). Located in the inner membrane and composed of approximately 25 copies of a single transmembrane protein, FliF, the MS-ring is the first circular structure to form during

flagellar assembly (Figure 1) (Macnab, 2003; Chevance *et al.,* 2008; Sowa, 2008). The MS-ring adheres to the switch complex through interactions mediated between the C-terminal tail of FliF ($FliF_C$) and the N-terminal region of FliG ($FliG_N$) (Francis *et al.,* 1992, Thomas *et al.,* 2001; Brown *et al.,* 2002; Grünenfelder *et al.,* 2003). Electron microscopy, site-directed alanine-scanning mutagenesis, and fusion/deletion studies have revealed that these two proteins directly interact with one another in a 1:1 stoichiometric ratio (Thomas *et al.,* 1999, 2001, 2006; Ogawa *et al.,* 2015). The structure of FliG has been determined for the full-length protein (Lee *et al.,* 2010), and the individual domains (Brown *et al.,* 2002, Minamino *et al.* 2011), alone and in complex with domains of FliM (Paul *et al.,* 2011; Vartanian *et al.,* 2012; Lam *et al.,* 2013; Sircar *et al.,* 2015). FliF is an integral membrane protein with extensive periplasmic domains homologous to the injectosome SctJ/D proteins and the sporulation factors SpoIIIAG/H (Bergeron, 2016). FliG and FliF orthologs are found in essentially all flagellated (and some non-flagellated) bacteria and thus this interaction can be considered a universal contact made in bacterial flagella (Levenson *et al.,* 2012; Bergeron, 2016).

To characterize the interaction between $FliF_C$ and $FliG_N$, Levenson *et al.* employed tryptophan fluorescence and ^{1}H-^{15}N TROSY-HSQC nuclear magnetic resonance spectroscopy to map the binding surface of *T. maritima* $FliF_C$ on $FliG_N$ (Levenson *et al.,* 2012). The K_d between $FliG_N$ and $FliF_C$ was measured in the low nanomolar range (< 40 nM) and $FliF_C$ binding caused chemical shift perturbations of backbone resonances across the entirety of $FliG_N$. As a whole, the data suggested that the $FliG_N$ domain orders as a result of $FliF_C$ binding – an effect consistent with multi-angle light scattering experiments that demonstrated the dissociation of FliG homodimers to form mixed $FliF_C$:FliG heterodimers upon $FliF_C$ addition (Levenson *et al.,* 2012). A strong interaction between $FliF_C$ and $FliG_N$ agrees well with previous observations made when purifying intact flagellar motors from *Salmonella* cells. Intact basal bodies readily lose the FliM and FliN regions of the C-ring; however, very low pH is required to induce dissociation of the FliF:FliG interface, owing to the unique strength of the interaction (Francis *et al.,* 1994). More recently, a similar interaction between FliF and FliG was reconstituted with a soluble full-length form of FliF from a marine *Vibro* species (Ogawa *et al.,* 2015).

Herein, we report the crystal structure of a complex between $FliF_{495–532}$ ($FliF_C$) and $FliG_{1–98}$ ($FliG_N$). All three domains of full-length FliG have a strikingly similar topology when $FliG_N$ is bound to $FliF_C$. Indeed, $FliG_N$ folds around the $FliF_C$ helices and produces a structure similar to that of the FliG middle domain ($FliG_M$) and the FliG C-terminal domain ($FliG_C$) (Brown *et al,* 2002; Lee *et al.,* 2010). Solution NMR, small-angle X-ray scattering (SAXS), and biochemical data are fully consistent with the structure, and help differentiate between two alternative complexes found in the crystal lattice. The $FliF_C$:$FliG_N$ structure was then used to model the MS/C-ring interface in the context of cryo-EM density for whole *Salmonella* rotors (Thomas *et al.,* 2006). An extended C-ring structure was generated taking into account previously placed $FliG_{MC}$:$FliM_M$ units (Sircar *et al.,* 2015). Targeted cross-linking and motility assays of structure-guided variant proteins reveal the functional importance of the $FliF_C$:$FliG_N$ interaction

Results

Solution-state properties of an engineered $FliF_C$:$FliG_N$ fusion protein

$FliF_C$:$FliG_N$ {$FliF_C$(495–532):$FliG_N$(1–98) for crystallography and $FliF_C$(495–532):$FliG_N$(1–102) for NMR} were produced as chimeric fusion proteins to ensure a 1:1 component ratio (SI Figure 1). The constructs were engineered such that FliG and FliF are linked together via a sequence containing a His_8 tag bracketed by two TEV protease sites (or one TEV protease site between His_8 and $FliG_N$ for the NMR studies). ^{1}H-^{15}N TROSY-HSQC NMR spectroscopy was employed to evaluate the resulting complex before and after TEV proteolysis (Figure 2B). Additionally, the cleaved complex was compared to that of ^{15}N labeled $FliG_N$ incubated with a synthetic $FliF_C$ peptide corresponding to the identical sequence encoded by the fusion construct (Figure 2A) (Levenson *et al.,* 2012) The ^{1}H-^{15}N TROSY-HSQC spectra of the $FliF_C$:$FliG_N$ fusion construct after TEV proteolysis (Figure 2A, red) is nearly identical to that of ^{15}N labeled $FliG_N$ incubated with stoichiometric amounts of the corresponding $FliF_C$ peptide (Figure 2A, black). Thus, the cleaved fusion protein has a conformation similar to that of $FliG_N$ mixed with $FliF_C$. Similarly, there are little differences in the measured ^{1}H-^{15}N resonances before (black) and after (red) TEV proteolysis (Figure 2B) indicating that the intact and cleaved proteins are remarkably similar in organization. Resonances of isotopically labeled TEV-proteolyzed $FliF_{495–532}$:$FliG_{1–102}$ complex were assigned using standard 3D NMR techniques, yielding assignments for 93% of residues (SI Figure 2A). Cα chemical shift deviations from random coil values showed both $FliF_{495–532}$ and $FliG_{1–102}$ within the complex to be well-folded, with alpha helical structure (SI Figure 2B). Overall, the data indicate the $FliF_C$:$FliG_N$ complex is the same whether produced as a fusion protein or as separate components and that the presence of a linker does not prevent complex assembly.

Solution-state structure of the $FliF_C$:$FliG_N$ complex by SAXS

SAXS was used to evaluate the $FliF_C$:$FliG_N$ solution-state structure. For these experiments, size-exclusion chromatography (SEC) was coupled to the SAXS measurements to separate different oligomeric or conformational states and limit contamination of soluble aggregates. The SEC chromatogram of the purified $FliF_C$:$FliG_N$ complex (SI Figure 3A) reveals a well-behaved protein complex. SAXS was measured for the area enclosed by the black dotted lines on the SEC chromatogram shown in SI Figure 3A. Kratky analysis of the scattering data (SI Figure 3B) converges towards zero at high q values, characteristic of a globular protein complex (Lipfert *et al.,* 2007). Generation of a low-resolution *de novo* molecular envelope of the protein complex results in a globular envelope with an extended region (SI Figure 3B). Interestingly, there appears to be poor agreement between the envelope and the structure of $FliG_N$ from a full-length FliG structure determined from *Aquifex aeolicus* (SI Figure 3D; Lee *et al.,* 2010). Either the binding of $FliF_C$ to $FliG_N$ produces a substantial conformational change in $FliG_N$ or the $FliF_C$ peptide is large enough to account for the unfilled area within the envelope. It is likely that FliF binding alters FliG, as the interaction converts FliG from a homodimer (FliG:FliG) to heterodimer (FliG:FliF) (Levenson *et al.,* 2012). For more information regarding SAXS data acquisition and envelope generation, see SI Methods.

Crystal Structure of $FliF_C$:$FliG_N$ complex

Crystals of the $FliF_C$:$FliG_N$ complex were grown by vapor diffusion at pH 7.5 (see Methods). Attempts to determine the structure of $FliF_C$:$FliG_N$ by molecular replacement (MR) failed, therefore a selenomethionine (seMet) variant of the $FliF_C$:$FliG_N$ complex was crystallized (see Methods). The seMet $FliF_C$:$FliG_N$ crystals diffracted to 2.6 Å resolution and yielded an initial SAD phased map with a figure of merit of 0.341. A *de novo* model was built and refined into the map with excellent final agreement statistics (Table 1). The unit cell consisted of two heterodimers per asymmetric unit, with one dimer having an extended α-helix towards the C-terminal portion of the FliG peptide, and the other having three segmented helices (Figure 3A). Although the two conformations of the last α-helix in $FliG_N$ may indicate flexibility of this helix, the dimer with the extended α-helix (Figure 3) agrees better with the SAXS envelopes and is thus presumed to represent the dominant solution-state structure (SI Figure 4C).

The $FliF_C$ terminal peptide forms two α-helices connected by a short extended linker (F_Cα1 residues 497–514, and F_Cα2 517–529, Figure 3B). $FliG_N$ is an all α-helical structure, similar to the all α-helical *T. maritima* $FliG_M$ and $FliG_C$ domains (Brown *et al.,* 2002; Paul *et al.,* 2011; Sircar *et al.,* 2015), as well as the full-length FliG from *A. aeolicus* (Lee *et al.,* 2010). $FliG_N$ consists of four helices, denoted G_Nα1–4 in Figure 3B (residues 6–19, 21–30, 33–45, and 51–87, respectively) where G_Nα1–3 form an ARM-like domain that is also present in $FliG_M$ and $FliG_C$ (Brown *et al.,* 2002; Lee *et al.,* 2010). Together with F_Cα2, G_Nα1–3 comprise a 4-membered right-handed super-helix that has been well-documented as a structural motif in other FliG structures (Brown *et al.,* 2002; Lee *et al.,* 2010; Paul *et al.,* 2011) and is also found in the N-terminal cytoplasmic domain of the Mg^{2+} transporter MgtE (Hattori *et al.,* 2007). We will refer to these FliG super-helical domains as ARM-like motifs, following previous designations ((Lee *et al.,* 2010; Vartanian *et al.,* 2012), although we note that these domains differ substantially from traditional ARM motifs in helix crossing angles and packing interactions (Andrade *et al.,* 2001). F_Cα1 and F_Cα2 assume a hook-like structure that latches into the V-shaped cavity formed from the G_Nα1–3 super helix and G_Nα4. In the unbound $FliG_N$ of *A. aeolicus* (Lee *et al.,* 2010), G_Nα1–3 forms a similar super helix but G_Nα4 is instead composed of two helices connected by a linker. Although similar in secondary structure, the unbound $FliG_N$ domain G_Nα4 from *A. aeolicus* does not superimpose as well with $FliG_N$ in complex with $FliF_C$ (SI Figure 4A). In the absence of $FliF_C$ this region may be highly flexible, which would explain the difficulty in crystallizing unbound $FliG_N$.

$FliF_C$ and $FliG_N$ associate to form a shared hydrophobic core. Interacting regions of $FliF_C$ and $FliG_N$ mapped by NMR involve the burial of conserved hydrophobic residues on both $FliF_C$ and $FliG_N$ (Levenson *et al.,* 2012). Similarly, the electrostatic potential at the molecular surface of $FliG_N$ reveals a hydrophobic, non-charged FliF binding region. The $FliF_C$:$FliG_N$ complex buries ~1,700 $Å^2$ of hydrophobic binding surface on the $FliF_C$ peptide, and is stabilized at the periphery by electrostatic interactions (SI Figure 5). A nearly invariant tryptophan residue essential for the $FliF_C$:$FliG_N$ interaction (*T. maritima* FliF W527) (Thomas *et al.,* 2001; Levenson *et al.,* 2012) is tightly sequestered within a hydrophobic pocket formed from G_Nα1, G_Nα4, and F_Cα2 (SI Figure 5E).

From the extensive hydrophobic interactions it appears as though $FliG_N$ folds around $FliF_C$. Surprisingly, the resulting topology matches that of the $FliG_M$ and $FliG_C$ domains (Figure 4A and 4B). The structure of the $FliF_C$:$FliG_N$ complex superimposes well with the tertiary structure of $FliG_M$ and $FliG_C$ from *T. maritima* (Figure 4; left - $FliG_M$ PDB: 3SOH, right - $FliG_C$ PDB: 1LKV), producing RMS values of 1.053 Å (40 residues) and 1.227 Å (63 residues), respectively (Paul *et al.,* 2011; Brown *et al.,* 2002). Superposition of the $FliF_C$:$FliG_N$ complex with the middle and C-terminal domains from *A. aeolicus* $FliG_{FL}$ results in a similar outcome (SI Figure 4) (Lee *et al.,* 2010).

Mapping of the $FliF_C$:$FliG_N$ interface by paramagnetic resonance enhancement

To further investigate the solution-state structure of the $FliF_C$:$FliG_N$ complex, paramagnetic relaxation enhancement (PRE) experiments were carried out in which ^{1}H-^{15}N TROSY-HSQC NMR spectra were collected on a $FliF_{495–532}$ (E508C):$FliG_{1–102}$ (*E. coli* FliF numbering) mutant that was conjugated to a MTSL nitroxide spin-label. Proximity to the conjugated MTSL causes neighboring ^{15}N backbone nuclei to experience increased resonance peak broadening. Mapping of the maximally broadened residues in $FliG_N$ from the spin label on $F_C\alpha1$ produces a binding interface that is in excellent agreement with the crystal structure (SI Figure 6 and SI Table 2). Notably, a small portion of the C-terminal tail of $G_N\alpha4$ also experiences a significant amount of resonance peak broadening with peak intensities 27–65% compared to that observed in the protein after the MTSL label had been reduced to a spectrally inactive form by addition of ascorbic acid, despite these residues being relatively far removed from the spin-label in the crystal structure. Perhaps the suspected flexibility of this helix brings it into proximity of the label for some conformational states of the complex.

Modeling of MS/C-Ring Interface of the Bacterial Flagellar Motor

The $FliF_C$:$FliG_N$ complex was then docked into 3D cryo-EM reconstructions of the intact CW locked *Salmonella* motors (Thomas *et al.,* 2006). It was assumed that the $FliF_C$ peptide descends perpendicular to the inner membrane, despite the 32-residue gap present between $F_C\alpha1$ and the second transmembrane helix (TM2) region of $FliF_{NM}$. Symmetric rings were generated that contained either 24, 25, or 26 copies of $FliF_C$:$FliG_N$, consistent with previously determined FliF:FliG stoichiometry (Thomas *et al.,* 2006). When $FliF_C$:$FliG_N$ rings with 24 or 26 subunits were docked into the C_{25} cryo-EM density, there were either clashes from overlapping secondary structural motifs (26 subunits), or unaccounted areas of electron density (24 subunits). Rings modeled with C_{25} symmetry had minimal steric clashes within the ring, minimized areas of unassigned density and produced a correlation coefficient of 0.83 to 30 Å resolution (Figure 5A–C). Thus, the dimensions of the $FliG_N$:$FliG_C$ complex agree well with the MS/C-ring symmetry. In modeling the MS/C-ring interface, $F_C\alpha1$ was directed upwards towards the inner-membrane, an orientation that conferred biological relevance, as well as allowed for systematic packing of all 25 subunits within minimal steric clashes (Figure 5A–C). In agreement with the model, recent bioinformatics-based modeling of the upper periplasmic region of $FliF_{NM}$ indicates 25 FliF subunits per MS-ring (Bergeron, 2016).

In an effort to extend the modeling further, we carried out the same fitting technique with a $FliG_{MC}$:$FliM_M$ complex structure previously generated via x-ray crystallography and pulse-dipolar ESR (PDB ID 4QRM, Sircar *et al.,* 2015). In total, 34 copies of a single $FliG_{MC}$:$FliM_M$ complex were fit into the rotor density, producing a correlation coefficient of 0.79 (Figure 5C). Notably there remains a disparity between the $FliG_{MC}$ and $FliG_N$ stoichiometry by 9 copies. This symmetry mismatch is well recognized (Thomas *et al.,* 1999, 2001; Manson, 2007; Berg 2003; Sowa *et al.,* 2008), and could result from unoccupied positions of $FliG_{MC}$ in the C-ring (Sircar *et al.,* 2015), non-equivalence in the FliG:FliM contacts (Paul *et al.*, 2011; Sakar *et al.,* 2011) or as a result of adaptive remodeling of both FliM and FliN (Fukuoka *et al.,* 1994; Lele *et al.,* 2012; Delalez *et al.*, 2014). Nonetheless, the current model suggests that 34 copies of FiG_N could not fit within the upper portion of the EM density.

Functional analysis of the $FliF_C$:$FliG_N$ complex

To validate the structure of $FliF_C$:$FliG_N$, site-directed mutants were evaluated by *in vivo* motility assays. All experiments were performed in *E. coli* with homologous *E. coli* proteins, where FliF and FliG share 29% and 36% sequence similarity with the *T. maritima* proteins, respectively, and conserve nearly all of the key residues involved in the complex interface (SI Figure 7) (Levenson *et al.,* 2012; Thomas *et al.*, 2001). Additionally, residue substitutions at the FliF-FliG interface were tested in protein interaction studies and crosslinking of engineered cysteine mutants were further employed to probe the functional FliF:FliG interface.

Hydrophobic to aspartate mutations FliG were made and cell migration rates were measured relative to wild type (Figure 6A,B). Residue substitutions along the FliF:FliG interface observed in the crystal structure proved most detrimental to motility. Specifically, motility defects were strongest for changes that are in close proximity to F_C α 2, especially at positions Leu13, Leu29, Leu37, Ile17 (*E. coli* numbering), which is consistent with the interactions between $FliF_C$ and FliG found in the crystal structure.

Analysis with the bacterial adenylate cyclase two-hybrid (BACTH) method provided independent support for a strong FliF:FliG interaction involving the interfaces observed in the crystal structure (Figure 6D) (Miller *et al.,* 1972; Karimova *et al.,* 2001; Battesti *et al.,* 2012). BACTH experiments used hybrid constructs containing the $FliF_C$ (*E. coli* residues 505–552) and $FliG_N$ (*E. coli* residues 1–87). In experiments with wild-type $FliF_C$ and $FliG_N$, strong color development was observed on MacConkey plates, and measurements of β-galactosidase activity afforded values comparable to the leucine-zipper positive control (Figure 6C). Hydrophobic-to-aspartate replacements of FliG on the predicted interface weakened the interaction in a pattern similar to the motility phenotypes. Residue substitutions made to FliF provided similar validation of the expected contact sites (SI Figure 8). These results suggest that the interface involving $F_C\alpha2$ may be chiefly responsible for the strength of the interaction. Consistent with this, a hydrophobic-to-aspartate replacement at FliF residue 542 in $F_C\alpha2$ eliminated both motility and the two-hybrid interaction. A mutation at position Val538 in $F_C\alpha1$ caused a significant reduction in migration rate, while not diminishing the FliF:FliG interaction. In liquid culture, this mutant

exhibited relatively weak motility and a substantial fraction of immotile cells, indicating a delay or partial defect in flagellar assembly. Thus, the V538D replacement alters the FliF:FliG relationship while not greatly weakening the interaction.

To further probe the FliF:FliG interaction *in vivo,* cross-linking of engineered cysteine mutants were employed to map the binding site interface between FliF and FliG in *E. coli.* Targeted disulfide crosslinking experiments indicate that the FliF:FliG relationship in *E. coli* is similar to that observed in the structure of the *T. maritima* proteins (Figure 7C). Fifty-five double-cysteine mutants were made (Figure 7A; SI Table 3). In total, seven relatively strong crosslinks were observed, all involving positions that are in proximity in the crystal structure (C_β-C_β distances 6–10.5 Å). All of the cysteine double mutants that displayed strong crosslinking retained significant function (45% – 85% of wild-type) in soft-agar. Crosslinking experiments yielded one surprising result; Cys543 in FliF showed only weak crosslinking though predicted to be close to several of the $FliG_N$ cysteine replacements. The strongest crosslink of Cys543 (still weak in absolute terms) was to Cys29 in FliG, which according to the structure is the closest (to 543) of the 11 FliG replacements examined. Residue 543, normally Ile, resides in $F_C\alpha1$ and is buried at the FliG:FliF interface. We hypothesized that packing in this region might be so stable as to prevent deprotonation or necessary movements of the buried cysteine side chains for crosslinking. In an attempt to loosen the interface and increase the reactivity of Cys543, the adjacent Arg544 was replaced with alanine; however, crosslinking was not significantly increased. Crosslinking was then carried out in the presence of urea (Figure 7B). The crosslink to FliG at Cys29 was slightly enhanced in the presence of 3 M urea, while crosslinking to a more distant position (Cys44) remained negligible.

Overall, results from the *in vivo* experiments fit well with the crystallographic structure of the $FliF_C$:$FliG_N$ complex, and indicate that the FliF:FliG interfaces are essentially identical in *E. coli* and *T. maritima*. As expected, the FliF:FliG interaction is critical for function. Mutant phenotypes and the non-reactivity of Cys543 highlight the importance of the interactions involving $F_C\alpha2$ and indicate that packing at this interface may be unusually stable.

Discussion

The MS/C-ring interface is an essential contact site of the flagellar motor. Not only does it serve as a checkpoint during flagellar morphogenesis, but it positions FliG with respect to the inner membrane such that it can (1) bind to the MS-ring to propagate rotation, (2) interact with the stator complexes to confer torque generation to the switch complex, and (3) position FliG such that it can bind to FliM to anchor CW/CCW switching and rotor dynamics (Berg, 2003; Sowa, 2008). Although fusion-deletion and mutagenesis studies have established that FliF and FliG interact through their N and C terminal domains, respectively, a molecular level view of this interaction remained elusive. The 2.1 Å resolution crystal structure of $FliF_C$:$FliG_N$ defines the interface between the MS and C-rings within the flagellar motor. Furthermore, by reconciling the $FliF_C$:$FliG_N$ crystal structure with NMR, SAXS, *in vivo* assays and modeling to cryo-EM reconstructions, we validate the structure as

biologically relevant and further expand current understanding of protein organization at the MS/C-ring interface.

Fusion of the $FliF_C$ peptide to $FliG_N$ was an effective strategy for producing the complex. Comparing TROSY-HSQC ^{1}H-^{15}N NMR spectroscopy of the fused protein to the complex formed by its components indicates that the fusion folds as the native complex (Figure 2). Given the intimate contact formed by the two separate proteins, it is not surprising that they appear to fold as one unit. Notably, the ability of the cleaved and non-cleaved moieties to form essentially the same structure places spatial restrictions on the location of the $FliF_C$ binding site. Fortunately, these restrictions were satisfied in the native $FliF_C$:$FliG_N$ complex (Figure 3), and found to be in agreement with the $FliF_C$:$FliG_N$ interface mapped from the PRE studies (SI Figure 6 and SI Table 2).

$FliF_C$:$FliG_N$ crystallizes in two conformations (Figure 3A). It was important to consider both when modeling the MS/C-ring interface. The $FliG_N$ core that houses the $FliF_C$ binding site remains invariant, owing to the strength of the FliF:FliG interaction. However, the C-terminal tail of $FliG_N$ ($G_N\alpha4$) assumes either an extended α-helix, or three segmented helices (Figure 3B). Although the crystal lattice may influence these conformations, the solution-state complex favors the extended helix (SI Figure 3B–C). Nonetheless, the more compact conformation may play a role in motor operation, as it confers a higher degree of flexibility thus could serve as a flexible hinge to absorb stress during rotation reversals. Modeling of the $FliF_C$:$FliG_N$ structure into the ring density (Figure 5A–B) directs $F_C\alpha1$ toward the inner membrane of TM2 of FliF. The 32 unaccounted residues between $FliF_C$ $F_C\alpha2$ and TM2 of $FliF_{NM}$ could similarly serve as a flexible hinge.

Importantly, $FliG_N$ requires $FliF_C$ to fold into a stable $FliG_M$/$FliG_C$-like domain, and thus the stoichiometry of FliF to FliG is most likely to be 1:1. Such a 1:1 complex has important implications for the overall structure of the rotor, as FliG must interact with FliM, of which there are ~34 copies. Therefore, either not every FliM interacts with one FliG in the same way, or the protein stoichiometry in the MS and C-rings are not correct. The latter seems unlikely, as 25 copies of the FliF:FliG complex fit well around the upper switch, and it is difficult to accommodate more subunits without significant steric clashes. Further, the current finding that the MS/C-ring interface has C_{25} symmetry is in agreement with recent homology modeling of the periplasmic region of FliF (Bergeron, 2016).

FliG is divided into three distinct domains, where each domain has evolved to carry out a specific function within the flagellar switch (Lloyd *et al.,* 1996; Berg, 2003; Sowa, 2008). $FliG_N$ contains the binding site for $FliF_C$ and anchors the C-ring to the inner-membrane, $FliG_M$ interacts with $FliG_C$ and $FliM_M$ to propagate CCW/CW switching, and $FliG_C$ contains conserved charged residues to interact with membrane-bound stators in torque generation (Lloyd *et al.,* 1997; Berg, 2003; Sowa, 2008). The structure of FliG determined from *A. aeolicus* agrees with structures of the M and C terminal domains (Brown *et al,* 2002; Paul *et al.,* 2002). A notable feature of unbound $FliG_N$ identified in the full-length structure was the structural similarity between $AqFliG_N$ helices N1–4, and $AqFliG_C$ terminal helices 3–6 (Lee *et al.,* 2010). A similar observation was made previously from the crystal structure of $FliG_{MC}$ from *T. maritima* (PDB 1LKV) regarding the ARM motifs present in $FliG_M$ and

$FliG_C$ ($ARM_{M/C}$) (Brown *et al.,* 2002). Interestingly, the $FliF_C$:$FliG_N$ complex shows how the structural replication within $FliG_C$ is even more extensive than in $FliG_{MC}$ (Figure 4; SI Figure 4). When FliF is bound to FliG, all three domains adopt similar conformations such that FliF:FliG aligns well with the ARM_M motif and $helix_{MC/NM}$ in $FliG_M$, as well as with helices 1–6 in $FliG_C$. The striking similarity of the FliF:FliG fold with that of $FliG_M$ and $FliG_C$ suggests domain shuffling may relate all three of the FliG domains (Di Roberto *et al.,* 2014). Either the N-terminal helix of $FliG_N$ was transferred to the C-terminus of FliF, or the $FliG_N$:$FliF_C$ unit was fused and propagated to generate $FliG_M$ and $FliG_C$. The genes for FliF and FliG are often adjacent, in the same orientation and expressed from the same promoter. Thus, in many instances the coding sequences for the two helices that complete the $FliG_N$ superhelix are tightly coupled to the FliG gene. Furthermore, in *Chlamydia* the C-terminal region of FliF has been replaced with an entire $FliG_M$-like domain (Bergeron, 2016). Thus, the interface between the FliF TM2 and the C-ring is always a $FliG_M$-like domain, whether it is composed of a single polypeptide or two that mate $FliF_C$ to $FliG_N$. Interestingly, upon comparing the sequences of the $FliF_C$:$FliG_N$ complex to $FliG_M$, the region where $FliF_C$ terminates and $FliG_N$ begins coincides with the $FliM_M$-binding EHPQR motif of $FliG_M$ (Paul *et al.,* 2011; Vartanian *et al.,* 2012) (Figure 4B). If $FliG_M$ and $FliF_C$:$FliG_N$ share a common origin, severing a continuous $FliG_N$ domain into two at what would be the FliM interaction site on the analogous $FliG_M$ may have been advantageous to prevent incorrect binding of $FliG_N$ to $FliM_M$ during MS/C-ring assembly.

The contact residues of the FliF:FliG structure mediate protein interactions in cells and are critical for generating functional flagella. Substitution of key hydrophobic residues to aspartic acid along the FliF:FliG interface of both FliG (Figure 6A) and FliF (SI Figure 8) disrupt cell motility and protein-interactions. Although $F_C\alpha1$ buries ~570 $Å^2$ of surface area, the functional specificity and strength of the FliF:FliG interaction can largely be attributed to $F_C\alpha2$. Disulfide crosslinking data provides direct biochemical evidence in support of these findings. One surprising observation was the relatively small extent of crosslink formation between buried FliF Cys543 and any potential disulfide partner (Figure 7B, SI Table 4). This result likely reflects the uniquely strong interaction between $F_C\alpha2$ and FliG that prevents movement of the cysteine residues or access to oxidants. These results provide evidence for the conjecture that $FliF_C$ and $FliG_N$ essentially fold as one domain to provide a robust anchor for the C-ring to the membrane. It is not surprising then that the FliF:FliG interaction is much stronger than that of the FliG:FliM or FliM:FliN and can persist longer at low pH without dissociation (Francis *et al*, 1994).

Overall, by combining data from x-ray crystallography, SAXS, NMR, modeling to cryo-EM structures and *in vivo* functional studies, we have defined the FliF:FliG interaction at the MS/C-ring interface. The structure has then been elaborated into an updated model for the upper switch. Importantly, the structure suggests that the FliF:FliG stoichiometry is likely the same, and that domain shuffling appears to have driven the association of these key building blocks of the flagellar motor. We propose a model where a domain is duplicated and then genetically split so that a folding unit can associate two otherwise non-interacting proteins with high affinity. It is notable that protein engineering has used a similar strategy of split protein complementation to effect interactions in cells through the development of tools such as split GFP, ubiquitin and luciferase proteins. (Xing *et al.*, 2016)

Experimental Procedures

i. Protein Expression and Purification

Native proteins were expressed in BL21 (DE3) *E. coli* cells, grown at 37°C in LB media containing 50 μg-mL^{-1} kanamycin, and induced with 1 mM Isopropyl β-D-1-thiogalactopyranoside (IPTG) at 25°C after reaching an OD_{600} of ~0.6. Selenomethionine variants were expressed in B834 methionine auxotrophic *E. coli* cells at 37°C in minimal media containing 100 μg-mL^{-1} ampicillin hydrochloride and 50 mg-L^{-1} +/− L-selenomethionine.

All proteins were purified according to the following procedure: cell pellets were re-suspended in lysis buffer (25 mM HEPES pH 7.5, 500 mM NaCl, 5 mM imidazole), lysed via sonication, and the lysate was then centrifuged at 20,000 rpm for 45 minutes at 4°C. The supernatant was passed through a Ni-NTA column, washed with 50 mL wash buffer (25 mM HEPES pH 7.5, 500 mM NaCl, 25 mM imidazole), and eluted with elution buffer (25 mM HEPES pH 7.5, 500 mM NaCl, 200 mM imidazole). The linker between $FliG_N$ and $FliF_C$ was removed by overnight incubation with TEV protease at 30°C. TEV was removed via centrifugation and the $FliF_C$:$FliG_N$ complex was dialyzed extensively against 50 mM sodium phosphate pH 6.5. For the preparation of selenomethionine $FliF_C$:$FliG_N$, all buffers were supplemented with 10 mM DTT. Successful selenomethionine incorporation was confirmed via whole-protein positive ion electrospray LC-MS/MS.

Crystallization, Data Collection, and Phasing—The $FliF_C$:$FliG_N$ complex was subjected to sparse course matrix screening in 600 nL drops at a protein concentration of 65 mg/mL. Crystals grew in 100 mM HEPES pH 7.5, 25% (w/v) PEG 3000, 200 mM NaCl at 25°C after ~7 days. Selenomethionine-incorporated crystals grew from 33 mg/mL protein, 100 mM imidazole pH 7.2, 130 mM NaCl, 30% (w/v) PEG 8000 in ~14 days.

Briefly, data sets were integrated and scaled in HKL2000 and SCALPACK (See Table 1). Phasing of the anomalous data set was done with Phenix HYSS and the model built with Autobuild (Phenix) programs (Adams *et al.*, 2010). Manual adjustments to model were made with COOT and subsequent refinements were carried out with Phenix Refine. The final $FliF_C$:$FliG_N$ model has an R_{free} of 21.74 % and a R_{work} of 16.92 % with excellent stereochemistry.

ii. Ring Simulation and Fitting into cryo-EM Maps

Low-resolution cryo-EM maps of whole rotor density containing the C, MS, L, and P rings were provided by Dennis Thomas (Thomas *et al.,* 2006). To construct a model of the upper C-ring/MS-ring interface, a single $FliF_C$:$FliG_N$ complex was aligned to the whole rotor density such that the coordinate systems of the crystal structure PDB file coincided with that of the rotor MRC map file. The center of mass was calculated for the placed complex, and the structure was duplicated *n* number of times and rotated 360/n degrees around an axis chosen perpendicular to the membrane. The ring was simulated to a radius of 15 nm, a distance corresponding to the radius of the EM map. Three rings of n = 24, 25 and 26 C_n fold symmetry were generated and evaluated with respect to the EM density. By inspection,

only rings of C_{25} fold symmetry produced a clash-free model that has minimal gaps in density when comparing. The C_{25} upper C/MS-ring model was fit into the EM map using the Fit to Map program in Chimera. When simulating the EM map to a resolution of 30 Å, the C_{25} fold $FliF_C$:$FliG_N$ ring provided good agreement with the whole rotor density and produced a correlation coefficient of 0.83. The above procedure was repeated with a $FliG_{MC}$:$FliM_M$ model (PDB 4QRM), to give a mid rotor subunit copy number of 34 and a correlation coefficient of 0.79.

iii. Generation, purification, and NMR analysis of isotopically enriched $FliF_C$:$FliG_N$ complex

The fusion $FliF_C$(495–532):$FliG_N$(1–102) construct was generated by traditional molecular cloning methods. The $FliF_C$ portion was amplified from a plasmid obtained from the JCSG and cloned into a plasmid containing $FliG_N$(1–102) (Levenson *et al.*, 2012). All NMR data was collected with a construct similar to SI Figure 1, however, the construct only included one TEV protease site between the His_8 tag and the $FliG_N$ domain. Isotopically-labeled proteins were grown in M9 minimal media supplemented with $^{15}NH_4Cl$, ^{13}C glucose, and/or D_2O (when necessary). Rosetta (DE3) *E. coli* cells were used for expression of all constructs. Cells were grown at 37 °C, and upon reaching an OD_{600} of ~0.6, were induced with a final concentration of 1 mM IPTG and expressed for approximately 6 hours. Purification was identical as described previously. After SEC, the protein samples were dialyzed into 50 mM sodium phosphate, 100 mM NaCl, pH 6.5 for NMR analysis. After dialysis, all samples were concentrated to their final concentration, at which point 0.02% (w/v) NaN_3 was added. NMR spectra were collected on a Bruker Avance 800 MHz spectrometer equipped with a cryoprobe.

E. coli strains and media for interaction and motility studies—*Escherichia coli* strains and plasmids are listed in SI Table 1. All strains were derivatives of the wild type strain RP437. Chromosomal in-frame deletions or point mutations were made by using the lambda red method (Datsenko *et al,* 2000). TB medium contained (per liter) 10 g tryptone and 5 g NaCl, LB medium contained the same plus 5 g yeast extract. Soft-agar motility plates used TB media and Bacto-agar at 2.6 g-liter^{-1}. Ampicillin was used at 100 μg-ml in liquid media, 100 μg-ml^{-1} in selective plates, and 50 μg-/ml^{-1} in soft-agar motility plates. Chloramphenicol was used at 50 μg-ml^{-1} in liquid media and selective plates and at 25 μg-ml^{-1} in motility plates. IPTG and sodium salicylate were prepared as aqueous 0.1 M and 10 mM stocks and used at the concentrations indicated in the figures.

iv. Motility assay

All of the experiments examining motility defects were carried out in the respective null backgrounds (DB225, EKS10, see SI Table 1). Soft-agar plates were spotted with 3 µl of overnight cultures. Once migration began, colony size was measured at regular intervals and plots of diameter vs. time fitted to a line to determine rates. Rates are reported relative to wild-type controls measured in the same experiment. Effects of Asp replacements on motility were measured in strains expressing the mutant FliG from a plasmid (derivatives of pKP619), induced with 100 µM IPTG. Effects of Asp replacements in FliF were measured in strains expressing FliF from the plasmid pEK16, induced with 0.3µM salicylate, and additionally expressing wild-type FliG from plasmid pKP619 (induced as above), in a Δ*fliF*

strain. The additional, plasmid-expressed FliG was found to be necessary for optimal function. Effects on motility of cysteine replacements in FliG and FliF were measured in a Δ*fliFfliG* double-deletion strain, with both proteins expressed from plasmids.

v. In vivo and crosslinking mutagenesis

Site-directed mutations were made using the QuikChange method (Stratagene). DNA sequencing and oligonucleotide synthesis were carried out by core facilities at the University of Utah.

vi. Double-cysteine cross-linking

Disulfide crosslinking between FliF and FliG was studied in strains expressing cysteine-containing FliG variants from the chromosome and cysteine-containing FliF variants from plasmid pEK16. For these experiments, wild type protein (FliF) was present along with the Cys-mutant FliF. Levels of the two were roughly equal. The plasmid was induced with 0.2 μM salicylate, which gave FliF levels sufficient to compete with the wild-type (cysteine-less) FliF expressed from the chromosome but not so high as to impair motility. (Motility impairment occurred with induction by 1 μM or higher.) Cells were cultured overnight at 37° C and diluted 100-fold into TB containing antibiotic and 0.2 μM sodium salicylate then grown at 32° C for 5–6 h (to OD_{600} 0.7 – 0.8). OD_{600} was measured to adjust the cell density, then equal numbers of cells were pelleted and re-suspended with XL buffer (20mM Na-phosphate pH7.4, 150mM NaCl). For cross linking with iodine, 0.1ml of cell mixed with 4 μl of 25 mM iodine for 3 min at room temperature, then sulfhydryl groups were blocked by addition of 2 μl 0.5 M NEM and incubation at room temperature for 3 min. Samples were mixed with an equal volume of 2X non-reducing loading buffer and heated at 95 °C for 10 min before loading on SDS-PAGE gels. Some experiments included urea during the cross-linking step, at the concentrations indicated in the figures, to test the effects of partially destabilizing the proteins.

vii. SDS page and immunoblotting

Proteins were resolved in 7.5% SDS-PAGE gels and transferred onto nitrocellulose using a Transblot turbo apparatus (BioRad). Rabbit polyclonal antibody against FliG was used at 1:1,000 dilution in a solution containing phosphate-buffered saline pH 7.4, 0.1% gelatin, and 0.01% sodium azide. Immunoblots were visualized and analyzed using the LiCor Odyssey infrared-imaging system.

viii. Two-hybrid interaction assay

Bacterial adenylate cyclase two-hybrid (BACTH) measurements of the FliF:FliG interaction used vectors provided in a kit from Euromedex. Procedures followed previously published procedures (Miller *et al.,* 1972; Battesti *et al.,* 2012) with minor modifications. Cells from a single colony were grown overnight at 32° C in LB containing ampicillin and 0.5 mM IPTG, then pelleted and re-suspended in PBS buffer. 0.04 ml of cells were mixed with 0.96 ml Z buffer (0.06 M Na_2HPO_4, 0.04 M NaH_2PO_4, 0.01 M KCl, 0.001 M $MgSO_4$, pH 7.0, 0.08% SDS, 0.22% (v/v) BME). Cells were permeabilized by addition 100 μl chloroform and vortexed for 10 sec, followed by incubation at 30° C for 5 min. Reaction was started by

adding 0.2 ml ONPG solution (4mg-ml^{-1}). After measured times of reaction at 30° C, reaction was stopped by addition of 0.5 ml 1 M $NaHCO_3$. Product was quantified by measurement of OD_{420}, with a correction due to cell scattering. Activity in Miller Units was computed according to the formula: {1000 × [(OD_{420} − 1.75 × OD_{550})]/(time of reaction × volume of culture used × OD_{600})}; where OD_{420} and OD_{550} are read from the reaction mixture and OD_{600} reflects cell density in the washed cell suspension.

Acknowledgments

Research reported in this publication was supported by the NIGMS of the NIH under Award Number T32GM008500 (MJL, BRC) and R01GM59544 (FWD). The content is solely the responsibility of the authors and does not necessarily represent the official views of the National Institutes of Health. We thank NECAT (NIH grant P41 GM103403) and CHESS/MacCHESS (NSF: DMR-1332208; NIH: P41 GM-103485) for access to data collection facilities.

References

Adams PD, et al. PHENIX: a comprehensive Python-based system for macromolecular structure solution. Acta Cryst. 2010; D66:213–221.

Andrade MA, Petosa C, O'Donoghue SI, Muller CW, Bork P. Comparison of ARM and HEAT protein repeats. Structure. 2001; 309:1–18.

Battesti A, Bouveret E. The bacterial two-hybrid system based on adenylate cyclase reconstitution in *Escherichia coli*. Methods. 2012; 5894:325–334.

Berg HC. The Rotary Motion of the Bacterial Flagella. Annu Rev Biochem. 2003; 72:19–54. [PubMed: 12500982]

Bergeron JR. Structural modeling of the flagellum MS ring protein FliF reveals similarities to the type III secretion system and sporulation complex. PeerJ. 2016; 4:e1718. [PubMed: 26925337]

Brown PN, Hill CP, Blair DF. Crystal structure of the middle and C-terminal domains of the flagellar rotor protein FliG. The EMBO Journal. 2002; 21:3225–3234. [PubMed: 12093724]

Chen S, Beeby M, Murphy GE, Leadbetter JR, Hendrixson DR, Briegel A, Jensen GJ. Structural diversity of bacterial flagellar motors. The EMBO Journal. 2011; 30:2972–2981. [PubMed: 21673657]

Chevance FFV, Hughes KT. Coordinating assembly of a bacterial macromolecular machine. Nature Reviews Microbiology. 2008; 6:455–465. [PubMed: 18483484]

Datsenko KA, Wanner BL. One-step inactivation of chromosomal genes in *Escherichia coli* K-12 using PCR products. Proc Natl Acad Sci USA. 2000; 97:6640–6645. [PubMed: 10829079]

Delalez NJ, Berry RM, Armitage JP. Stoichiometry and Turnover of the Bacterial Flagellar Switch Protein FliN. mBio. 2014; 5:e01216. [PubMed: 24987089]

Di Roberto RB, Peisajovich SG. The role of domain shuffling in the evolution of signaling networks. Journal of Experimental Zoology Part B, Molecular and Developmental Evolution. 2014; 322:65–72.

Francis NR, Irikura VM, Yamaguchi S, DeRosier DJ, Macnab RM. Localization of the Salmonella typhimurium flagellar switch protein FliG to the cytoplasmic M-ring face of the basal body. Proc Natl Acad Sci USA. 1992; 89:6304–6308. [PubMed: 1631122]

Francis NR, Sosinsky GE, Thomas D, DeRosier DJ. Isolation, characterization and structure of bacterial flagellar motors containing the switch complex. Journal of Molecular Biology. 1994; 235:1261–70. [PubMed: 8308888]

Fukuoka H, Inoue Y, Terasawa S, Takahashi H, Ishijima A. Exchange of rotor components in functioning bacterial flagellar motor. Biochemical and Biophysical Research Comm. 2010; 394:130–135.

Grünenfelder B, Gehrig S, Jenal U. Role of the cytoplasmic C terminus of the FliF motor protein in flagellar assembly and rotation. Journal of Bacteriology. 2003; 185:1624–1633. [PubMed: 12591880]

Hattori M, Tanaka Y, Fukai S, Ishitani R, Nureki O. Crystal structure of the MgtE Mg2+ transporter. Nature. 2007; 448:1072–1076. [PubMed: 17700703]

Karimova G, Ullmann A, Ladant D. Protein-protein interaction between *Bacillus stearothermophilus* tyrosyl-tRNA synthetase subdomains revealed by a bacterial two-hybrid system. J Mol Microbial Biotechnol. 2001; 3:73–82.

Lam KH, et al. Structural basis of FliG-FliM interaction in Helicobacter pylori. Molecular Microbiology. 2013; 88:798–812. [PubMed: 23614777]

Lee LK, Ginsburg MA, Crovace C, Donohoe M, Stock D. Structure of the torque ring of the flagellar motor and the molecular basis for rotational switching. Nature. 2010; 466:996–1000. [PubMed: 20676082]

Lele PP, Branch RW, Nathan VSJ, Berg HC. Mechanism for adaptive remodeling of the bacterial flagellar switch. Proc Natl Acad Sci USA. 2012; 109:20018–20022. [PubMed: 23169659]

Levenson R, Zhou H, Dahlquist FW. Structural insights into the interaction between the bacterial flagellar motor proteins FliF and FliG. Biochemistry. 2012; 51:5052–5060. [PubMed: 22670715]

Lipfert J, Doniach S. Small-Angle X-Ray Scattering from RNA, Proteins, and Protein Complexes. Annual Review of Biophysics and Biomolecular Structure. 2007; 36:307–327.

Lloyd SA, Blair DF. Charged residues of the rotor protein FliG essential for torque generation in the flagellar motor of Escherichia coli. Journal of Molecular Biology. 1997; 266:733–744. [PubMed: 9102466]

Lloyd SA, Tang H, Wang X, Billings S, Blair DF. Torque generation in the flagellar motor of Escherichia coli: evidence of a direct role for FliG but not for FliM or FliN. Journal of Bacteriology. 1996; 178:223–231. [PubMed: 8550421]

Macnab RM. How Bacteria Assemble Flagella. Annual Review of Microbiology. 2003; 57:77–100.

Manson MD. How 34 pegs fit into 26 + 8 holes in the flagellar motor. Journal of Bacteriology. 2007; 189:291–293. [PubMed: 17085552]

Miller, JH. Experiments in molecular genetics: Assay of β-Galactosidase. Cold Spring Harbor Laboratory press; Cold Spring Harbor NY: 1972. p. 352-355.

Minamino T, Imada K. The bacterial flagellar motor and its structural diversity. Trends in Microbiology. 2015; 23:267–274. [PubMed: 25613993]

Minamino T, Imada K, Kinoshita M, Nakamura S, Morimoto YV, Namba K. Structural Insight into the Rotational Switching Mechanism of the Bacterial Flagellar Motor. PLoS Biology. 2011; 9:e1000616. [PubMed: 21572987]

Minamino T, Imada K, Namba K. Molecular motors of the bacterial flagella. Current Opinion in Structural Biology. 2008; 18:693–701. [PubMed: 18848888]

Ogawa R, Abe-Yoshizumi R, Kishi T, Homma M, Kojima S. Interaction of the C-terminal tail of FliF with FliG from the Na+-driven flagellar motor of Vibrio alginolyticus. Journal of Bacteriology. 2015; 197:63–72. [PubMed: 25313387]

Paul K, Gonzalez-Bonet G, Bilwes AM, Crane BR, Blair D. Architecture of the flagellar rotor. The EMBO Journal. 2011; 30:2962–2971. [PubMed: 21673656]

Sarkar MK, Paul K, Blair DF. Subunit organization and reversal-associated movements in the flagellar switch of Escherichia coli. Journal of Biological Chemistry. 2010; 285:675–684. [PubMed: 19858188]

Sircar R, Borbat PP, Lynch MJ, Bhatnagar J, Beyersdorf MS, Halkides CJ, Crane BR. Assembly States of FliM and FliG within the Flagellar Switch Complex. Journal of Molecular Biology. 2015; 427:867–886. [PubMed: 25536293]

Sowa Y, Berry RM. Bacterial flagellar motor. Quarterly Reviews of Biophysics. 2008; 41:103–132. [PubMed: 18812014]

Thomas DR, Francis NR, Xu C, DeRosier DJ. The three-dimensional structure of the flagellar rotor from a clockwise-locked mutant of Salmonella enterica serovar Typhimurium. Journal of Bacteriology. 2006; 188:7039–48. [PubMed: 17015643]

Thomas DR, Morgan DG, DeRosier DJ. Rotational symmetry of the C ring and a mechanism for the flagellar rotary motor. Proc Natl Acad Sci USA. 1999; 96:10134–10139. [PubMed: 10468575]

Thomas D, Morgan DG, DeRosier DJ. Structures of bacterial flagellar motors from two FliF-FliG gene fusion mutants. Journal of Bacteriology. 2001; 183:6404–6412. [PubMed: 11591685]

Vartanian AS, Paz A, Fortgang EA, Abramson J, Dahlquist FW. Structure of flagellar motor proteins in complex allows for insights into motor structure and switching. Journal of Biological Chemistry. 2012; 287:35779–35783. [PubMed: 22896702]

Xing S, Wallmeroth N, Berendzen KW, Grefen C. Techniques for the Analysis of Protein-Protein Interactions in Vivo. Plant Physiology. 2016; 171:727–758. [PubMed: 27208310]

Highlights

- $FliF_C$:$FliG_N$ fold together to produce a topology that repeats throughout FliG
- $FliF_C$:$FliG_N$ interact through hydrophobic contacts critical for motor function
- FliF:FliG 1:1 stoichiometry produces an MS/C-ring interface with ~C_{25}-fold symmetry

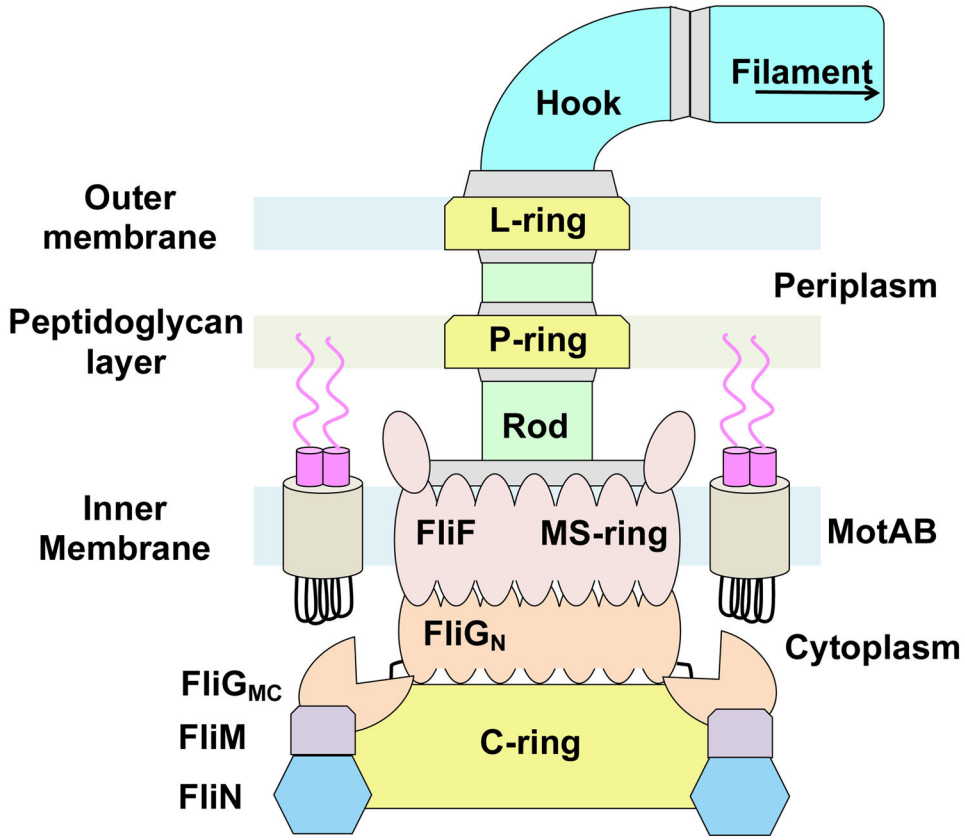

Figure 1.
Schematic diagram of the bacterial flagellar motor.

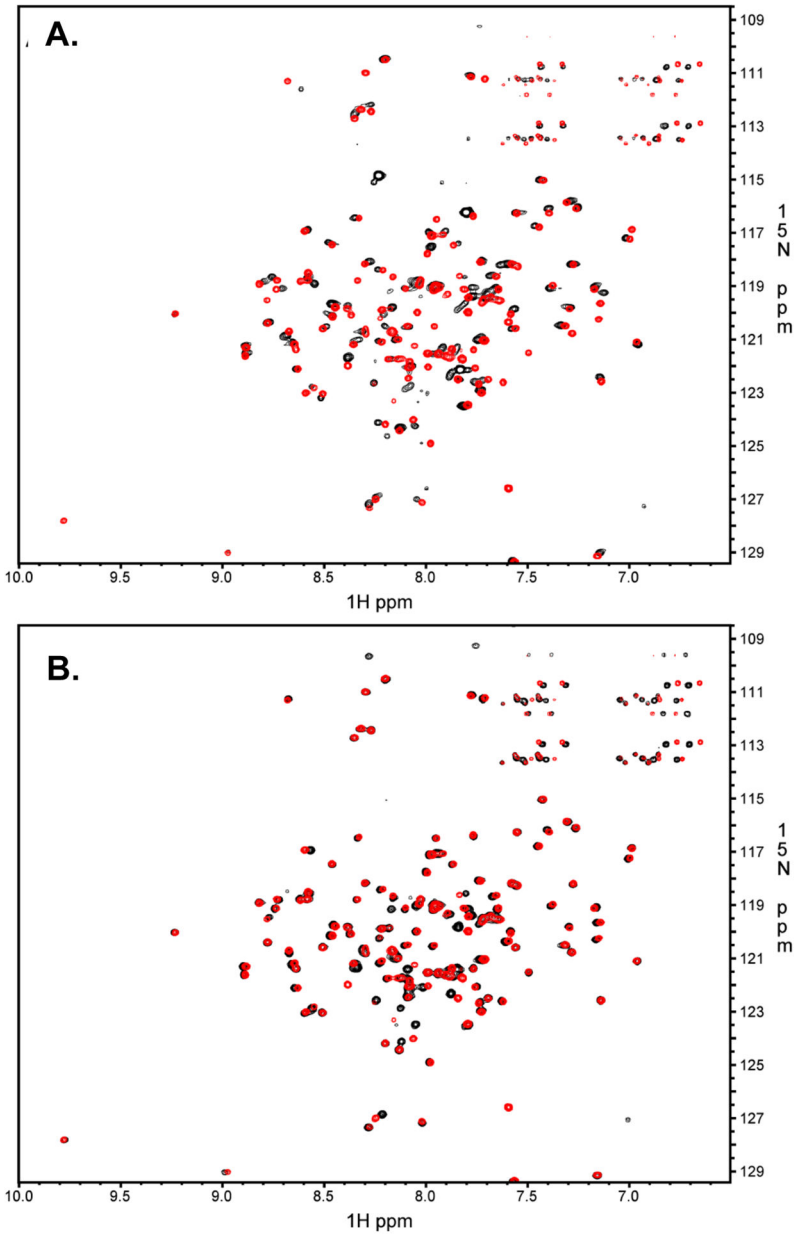

Figure 2.

NMR Characterization of $FliF_{495–532}$:$FliG_{1–102}$ complex. **(A)** Black: TROSY-HSQC data of ^{15}N-labeled $FliG_{1–102}$ bound to unlabeled $FliF_{495–532}$ peptide. Red: TROSY-HSQC data of ^{15}N-labeled $FliF_{495–532}$:$FliG_{1–102}$ fusion protein after TEV proteolysis. **(B)** Black: TROSY-HSQC data of ^{15}N-labeled $FliF_{495–532}$:$FliG_{1–102}$ fusion protein before TEV proteolysis Red: TROSY-HSQC data of ^{15}N-labeled $FliF_{495–532}$:$FliG_{1–102}$ fusion protein after TEV proteolysis. See also SI Figures 1, 2 and 6.

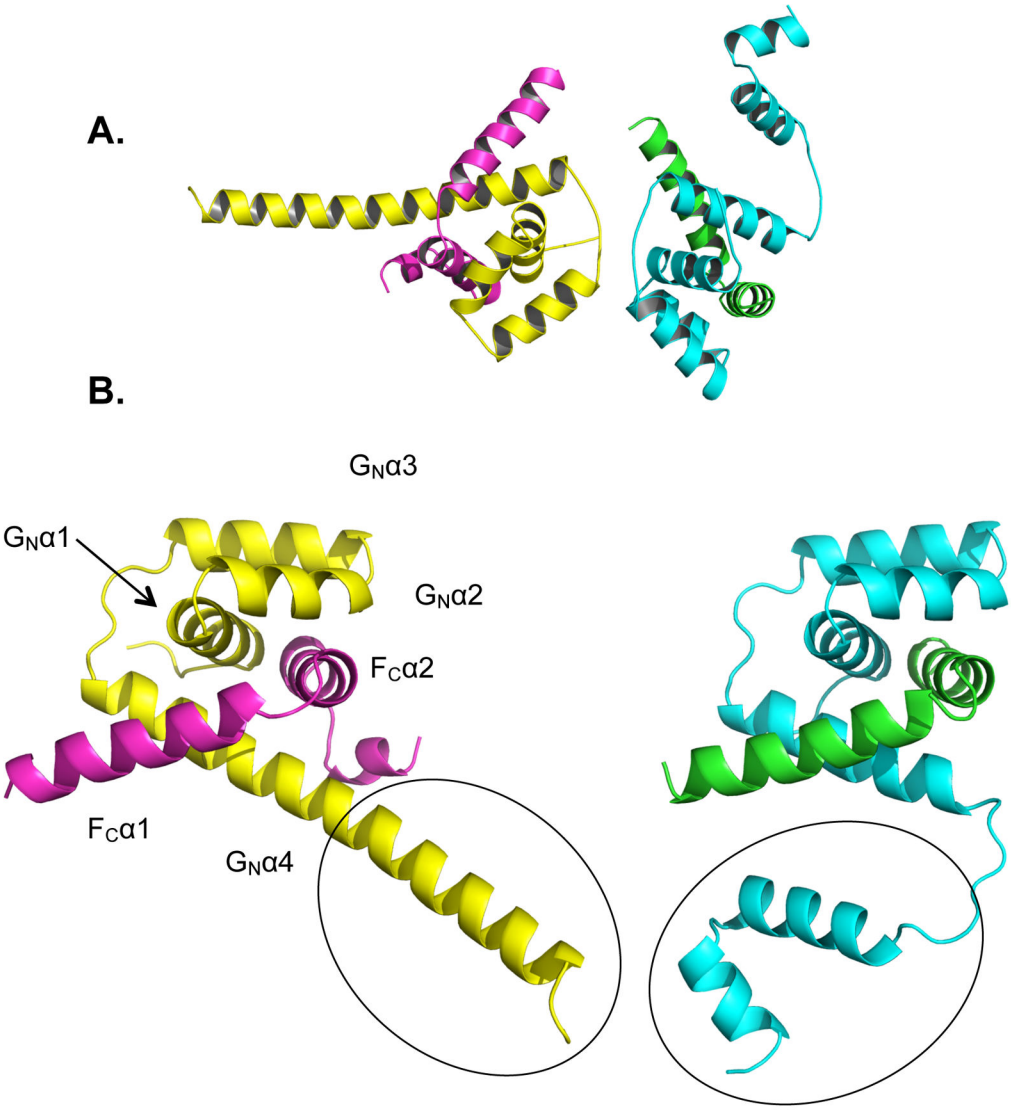

Figure 3.

Crystal Structure of $FliF_C$:$FliG_N$. The two unique heterodimers per asymmetric unit oriented as in the crystal **(A)** or with the same perspective **(B)** ($FliF_C$ - violet and green, $FliG_N$ - yellow and cyan). The two different morphologies of the terminal $FliG_N$ helix are circled. See also SI Figures 3, 5, 6, and 7.

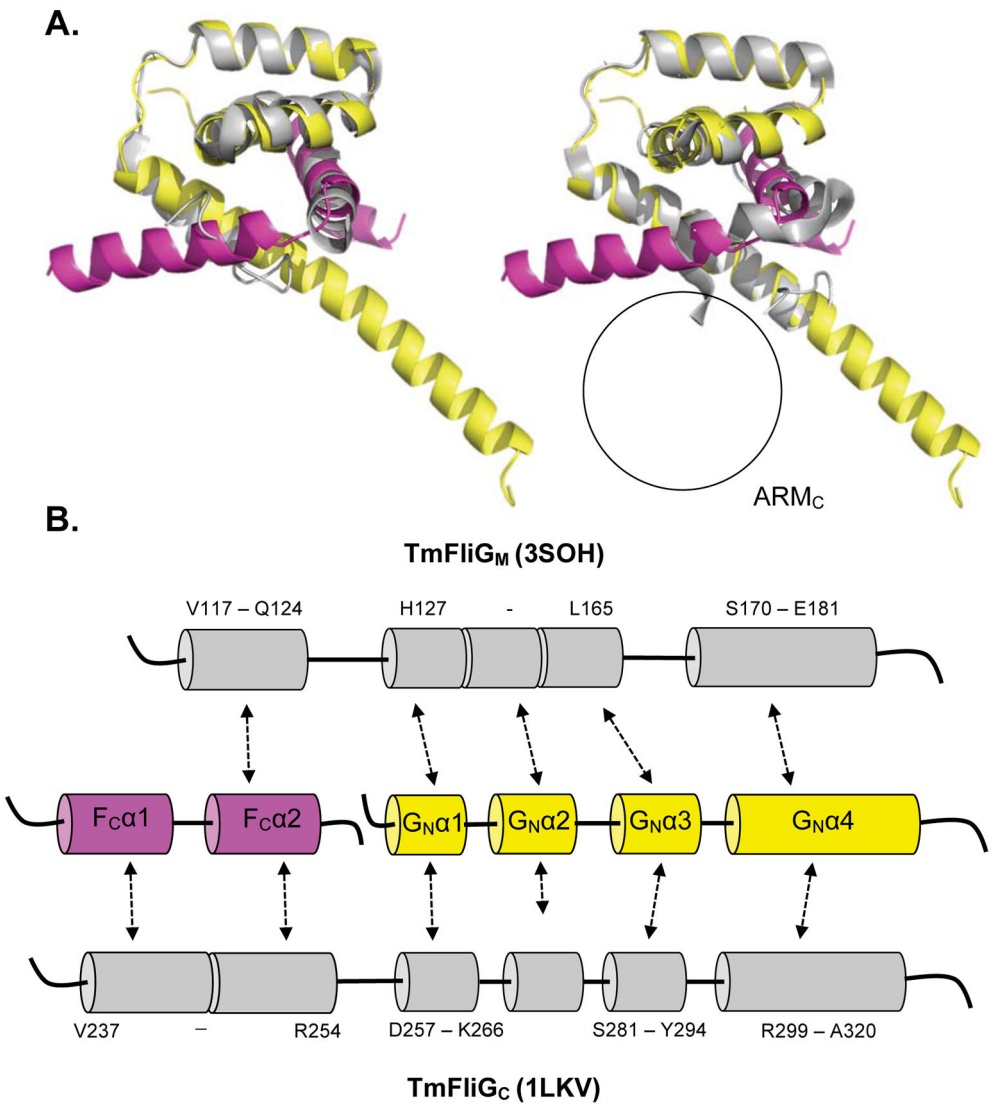

Figure 4.

Domain repeats within FliG. **(A)** Superimposition of *T. maritima* $FliF_C$:$FliG_N$ complex ($FliF_C$ - violet, $FliG_N$ - yellow) and *Thermotoga maritima* (left) $FliG_M$ (grey, PDB 3SOH, RMS 1.053 Å, 40 residues) and (right) $FliG_C$ (grey, PDB 1LKV, RMS 1.227 Å, 63 residues). The black circle signifies the absence of a corresponding ARM_C domain. **(B)** Comparison of secondary structure motifs and primary sequence alignment of the superimposed regions. See also SI Figure 4.

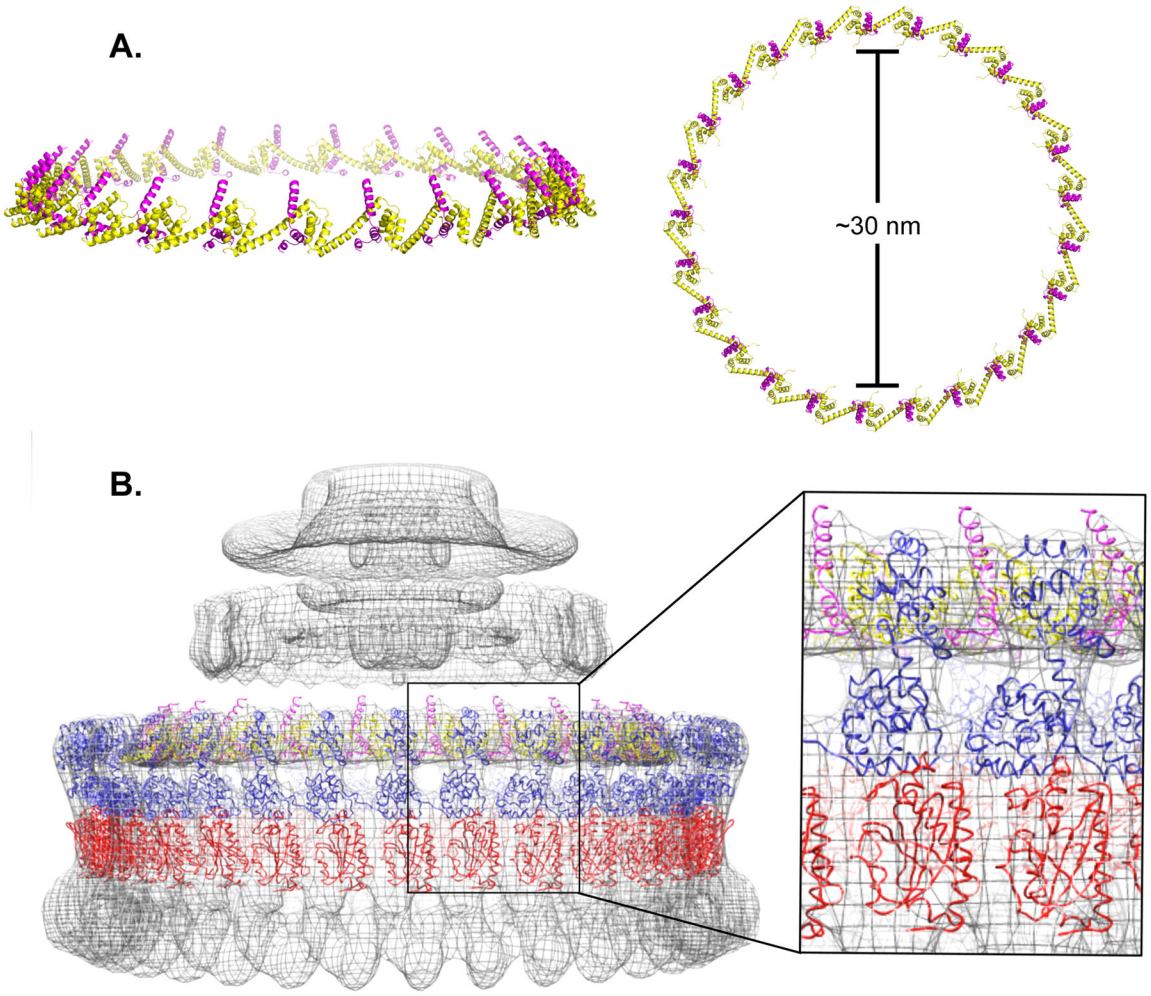

Figure 5.

Modeling of the $FliF_C$:$FliG_N$ ring with C_{25} symmetry. **(A)** Fully assembled $(FliF_C:FliG_N)_n$ ring (n = 25 copies) showing the side (left) and top (right) view. **(B)** $(FliF_C:FiG_N)_{25}$ ring and $(FliM_M:FliG_{MC})_{34}$ ring, (red -$FliM_M$, blue -$FliG_{MC}$) superimposed with the EM density of the *Salmonella* rotor (Thomas *et al.,* 2006) Ring density simulated at a 30 Å from the structures gave correlation coefficients with the EM density as follows: ($FliF_C$:FliGN) 0.83, and ($FliM_M$:$FliG_{MC}$) 0.79.

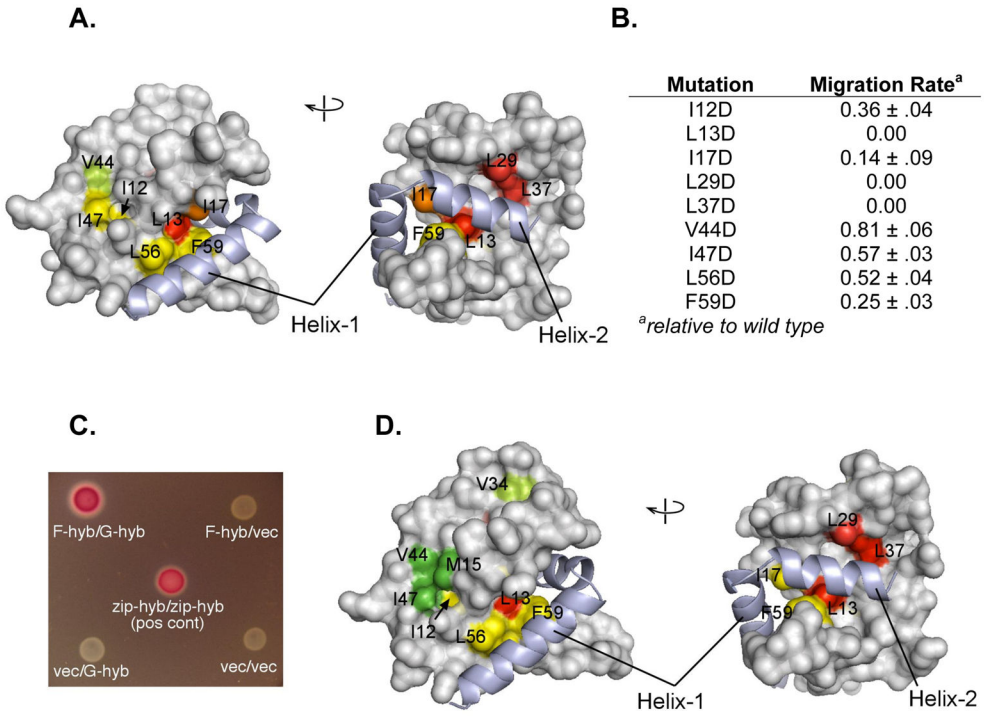

Mutation	Migration Rate[a]
I12D	0.36 ± .04
L13D	0.00
I17D	0.14 ± .09
L29D	0.00
L37D	0.00
V44D	0.81 ± .06
I47D	0.57 ± .03
L56D	0.52 ± .04
F59D	0.25 ± .03

[a]*relative to wild type*

Figure 6.

In vivo E. coli motility and interaction assays. **(A)** Two views of the $FliG_N$ domain, showing motility defects that result upon replacement of the indicated hydrophobic residues with aspartate. Motility phenotypes were tested by expressing mutant FliG proteins in the fliG null strain. Yellow-green, rate less than 100% but greater than 70% of wild-type; yellow, rate between 20% and 70% of wild type; orange, motile but at less than 20% of wild type; red, immotile. **(B)** A table summarizing the relative rates, values are the mean ± s.d. for 3 determinations. **(C)** Interaction between $FliF_C$ (residues 505–552) and $FliG_N$ (residues 1–87) observed in the bacterial adenylate cyclase two-hybrid system. Positive interactions drive expression of β-galactosidase. Negative controls and a leucine-zipper positive control are shown. **(D)** Effects of hydrophobic-to-aspartate replacements in $FliG_N$ on the FliF-FliG interaction. Coloring is based on β-galactosidase activities: Green, activity indistinguishable from wild type; yellow-green, activity less than 100% but greater than 70% of wild type; yellow, activity between 20% and 70% of wild type; red, activity decreased to the level of negative controls. $FliF_C$ shown light purple in all figures. See also SI Figure 8.

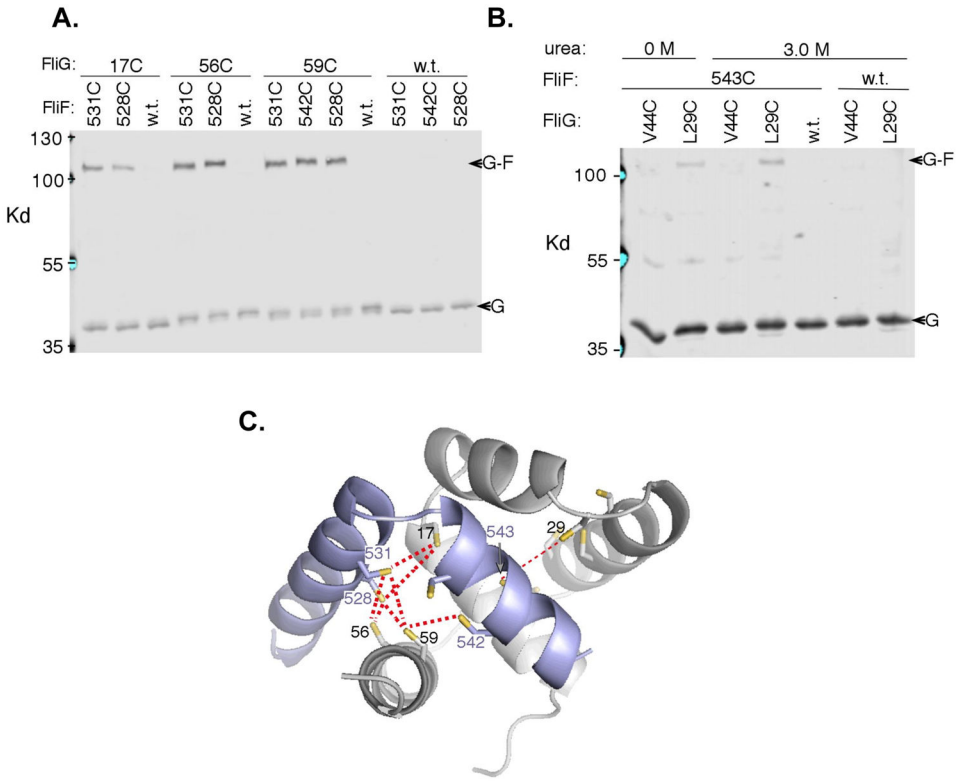

Figure 7.

In vivo FliG-FliF crosslinking. **(A)** Products of iodine-induced disulfide crosslinking were detected using anti-FliG immunoblots. The seven cysteine pairs that gave strong crosslinking are shown together with single cysteine controls. Crosslinking was weak or undetectable for forty-eight other cysteine pairs tested (SI Table 3). In addition to the indicated cys-mutant FliF, a comparable amount of wild-type FliF (expressed from the chromosome) was present in the crosslinking experiments; thus, crosslinking yields should underestimate what would occur if all of the FliF carried the Cys replacement. **(B)** A low-yield crosslink between FliG position 543 and FliG position 29 that is made somewhat stronger (by ~50%) in the presence of 3 M urea. The more-distant position Cys44 did not crosslink. **(C)** Mapping the crosslinks onto the FliG-FliF structure. Thicker red lines indicate the crosslinks observed under standard conditions, and the thin red line indicates the weaker, urea-enhanced crosslink involving the buried position 543. See also SI Figure 8.

Table 1

Data collection and Refinement Statistics

	Wild Type $FliF_C$:$FliG_N$ complex	Selenomethionine $FliF_C$:$FliG_N$ complex
Wavelength (Å)	0.97700	0.97921
Synchrotron	CHESS[a]	APS[b]
Beam-line	A1	24-ID-E
Space group	$P2_1$	$P2_1$
a, b, c (Å)	49.18, 59.33, 51.72	48.81, 59.24, 51.76
α, β, γ (°)	90.00, 115.59, 90.00	90.00, 115.76, 90.00
Resolution (Å)	50.0 - 2.10 (2.15 - 2.10)	50.0 - 2.60 (2.66 - 2.60)
$^{\dagger}R_{merge}$ (%)	8.2	12.2
$^{\dagger}R_{p.i.m.}$ (%)	5.5 (21.8)	5.3 (15.8)
$^{\dagger}R_{meas}$ (%)	9.9 (35.5)	13.3 (38.8)
■$I/\sigma(I)$■	13.4 (3.2)	14.8 (7.0)
Completeness (%)	99.5 (99.6)	99.2 (99.5)
Multiplicity	3.1 (2.4)	6.0 (6.0)
Anomalous completeness (%)		98.1
Mosaicity	0.43 – 0.81	0.63 – 2.55
Total Reflections	47,958	46, 599
Phaser FOM		0.341
Refinement		
Resolution (Å)		44.35 - 2.10 (2.18–2.10)
No. of unique reflections		15,618 (1559)
Reflections used for R_{free}		1556 (161)
R_{work}/R_{free} (%)		16.9 (17.4)/21.7 (23.7)
Clash Score		4.70
No. of non-hydrogen atoms		2263
Protein		2090 (260 residues)
Water		173
***B* factors (Å^2)**		
Wilson		18.1
Average B-factors		24.3
Protein		23.7
Water		31.8
R.M.S. deviations		
Bond lengths (Å)		0.007
Bond angles (°)		0.9
Ramachandran outliers (%)		0.4
Rotamer outliers (%)		1.3

Statistics for the highest-resolution shell are shown in parenthesis,

$^{\dagger}R_i = \Sigma\Sigma_i|I_i - \langle I_i \rangle| / \Sigma\Sigma_i I_i$

[a]Cornell High Energy Synchrotron Source - Cornell University

[b]Advanced Photon Source - Argonne National Lab